A 3-D Field Solution for Axially Polarized Multi-Pole Ring Permanent Magnets and its Application in Position Measurement

Eric A. Ponce and Steven B. Leeb, *Fellow, IEEE*

Massachusetts Institute of Technology, Cambridge, MA 02139 USA

Axially polarized multi-pole ring permanent magnets are industrially valuable in the construction of sensors and actuators. Available analytic field solutions for these magnets typically provide spatially incomplete or imaginary-valued results that do not reflect real-world measurement. This article presents simplified and real-valued 3-D field solutions for axially polarized ring magnets. The individual components are expressed in terms of elementary functions and incomplete elliptic integrals for easy evaluation with standard scientific computing libraries. These models are employed to analyze the effects of nonidealities in magnetic position systems. Demonstrations are offered through simulation and experimental measurement of two real-world ring permanent magnets, along with comparisons to prior models.

Index Terms—**Analytical calculation, axial magnetization, magnetic system design, permanent magnet.**

I. INTRODUCTION

CYLINDRICAL permanent magnets find wide use in electromechanical and mechanical applications. Commercially important systems such as permanent magnet motors, magnetic couplers, and position sensors use axially and diametrically polarized cylindrical magnets. Multi-pole magnets, comprising alternating polarity cylindrical sectors, produce magnetic fields convenient for coupling to other magnetic fields and space-alternating field components useful for position and angle sensing. Analytical field solutions for these magnets can be used for optimizing parameters and estimating performance characteristics of the design or measurement of systems. For position measurement, analytical solutions can be used to estimate the effects of misalignment or magnetization asymmetries when designing and using measurement systems.

The field solution for such magnets has been extensively studied in 3-D space, with a wide range of solution techniques. As examples of the body of work examining axially polarized ring magnets, consider [1]–[9]. Ravaud *et al.* [1], [2] provide a solution for axially and radially polarized cylindrical ring sectors using magnetic pole surface densities and the Coulombian model, ultimately producing field solutions in complex-valued elliptic integral and inverse hyperbolic form that encompasses the entire space around the magnet but results in imaginary-valued numerical error that does not reflect real-valued lab measurements. Ausserlechner [7] employed the equivalent current sheet method and assumptions about the geometry of an axially polarized ring magnetic encoder (ME) to calculate simpler analytic expressions that are approximately correct only in the near-field and then used

them to provide insights into the designing of magnetic position sensing systems. Furlani and Knewtson [8] also presented a numerical 3-D field solution for axially polarized disks using the equivalent current sheet method and Simpson's method for numerical integration of the magnetic vector potential [9]. This model is then extended for use in axial-field permanent-magnet motors using the method of magnetic images for compensating for high-permeability materials in the motor construction [8]. These models are compared against finite-element analysis (FEA) techniques for a variety of magnetic disk configurations. Relatedly, although not constrained to permanent magnets, Urankar [10] presented real-valued analytic solutions to current-carrying arc segments and provided simplified solutions for thin-sheet cylinders which may be used for computing the field from a single-pole pair magnetic ring.

This article seeks a closed form and physically accurate solution that covers the entire space around such a magnet. Such a solution provides an avenue for near real-time applications, such as *in situ* parameter estimation for calibration, measurement, or control applications, as well as other analytic optimization techniques that may not be easily or accurately achieved with FEA alone, especially in computationally constrained systems.

Specifically, this article presents a simple, closed form, and real-valued form of the 3-D field solution for axially polarized ring permanent magnet sectors that can be accurately and quickly evaluated using widely available scientific computing libraries for the applications mentioned above. It is then used to analyze the characteristics of the field and how they may be exploited in measurement applications and is verified against real-world measurements and previous results.

II. ANALYTICAL FORMULATION

An axially polarized ring permanent magnet with large coercivity and homogeneous magnetization may be modeled as a collection of surface currents using the equivalent current
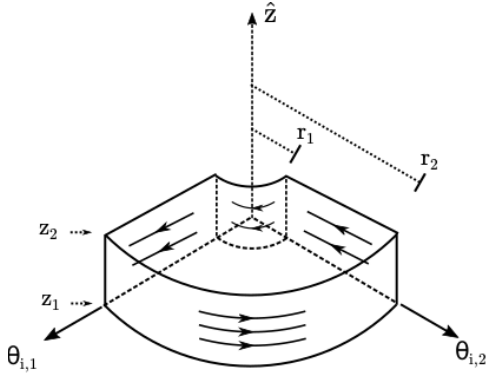
Fig. 1. Cylindrical magnet sector geometry (surface currents for axial polarization indicated with arrows).

sheet method [7]. The ring is divided into cylindrical pole-pair sectors and modeled as a set of surface currents running along the bounds of the sector parallel to the polarization direction. The field contribution from these surface currents can be calculated using the Biot–Savart law and superimposed to compute the complete field solution in 3-D space.

A. Geometry and Approach

The study begins by dividing the ring's geometry into single pole-pair cylindrical sectors with constant surface currents running around the perimeter of the sector and parallel to the axial direction $\widehat{z}$, as shown in Fig. 1. A cylindrical sector i spans $(r_1 \leq r \leq r_2; \theta_{i,1} \leq \theta \leq \theta_{i,2}; z_1 \leq z \leq z_2)$ and is composed of six bounding segments. In cylindrical coordinates, the surface currents point in one constant direction: $\widehat{r}$ along the radial segments and $\widehat{\theta}$ along the arc segments. Taking these surface currents into account and the appropriate form of the Biot–Savart law produce surface integrals representing the field contribution from each type of the segment. For a radial segment at $\theta = \theta_i$, the field solution can be found by integrating

$$\vec{B}_{i,\mathrm{rad}}^{\mathrm{seg}}(\vec{r}) = \frac{\mu_0}{4\pi} \int_{z_1}^{z_2} \int_{r_1}^{r_2} \cdot \vec{f}_{\mathrm{rad}}(\vec{r}; \vec{r}')G(\vec{r}; \vec{r}')^3 \, dr' \, dz' \Big|_{\theta'=\theta_i} \quad (1)$$

where μ_0 is the vacuum magnetic permeability and $\vec{f}_{\mathrm{rad}}(\vec{r}; \vec{r}')$ is the result of taking the vector product between the modeled surface current and the displacement vector $(\vec{r} - \vec{r}')$ in a cylindrical coordinate basis, leading to

$$\vec{f}_{\mathrm{rad}}(\vec{r}; \vec{r}') = -\zeta \sin \varphi \, \widehat{r} - \zeta \cos \varphi \, \widehat{\theta} + r \sin \varphi \, \widehat{z} \quad (2)$$

with $\varphi = (\theta - \theta')$, $\zeta = (z - z')$ and $G(\vec{r}; \vec{r}')$ being Green's function for cylindrical coordinate input vectors, or the inverse magnitude of the displacement vector

$$G(\vec{r}; \vec{r}') = \frac{1}{|\vec{r} - \vec{r}'|} = \frac{1}{\sqrt{r^2 + r'^2 + \zeta^2 - 2rr' \cos \varphi}}. \quad (3)$$

For an arc segment i at $r = r_j$ and spanning $\theta_{i,1} \leq \theta \leq \theta_{i,2}$, the field solution is similarly found by solving

$$\vec{B}_{i,j,\mathrm{arc}}^{\mathrm{seg}}(\vec{r}) = \frac{\mu_0}{4\pi} \int_{z_1}^{z_2} \int_{\theta_{i,1}}^{\theta_{i,2}}$$
$$\cdot \vec{f}_{\mathrm{arc}}(\vec{r}; \vec{r}')G(\vec{r}; \vec{r}')^3 r' \, d\theta' \, dz' \Big|_{r'=r_j} \quad (4)$$

with

$$\vec{f}_{\mathrm{arc}}(\vec{r}; \vec{r}') = \zeta \cos \varphi \, \widehat{r} - \zeta \sin \varphi \, \widehat{\theta} + (r' - r \cos \varphi) \, \widehat{z}. \quad (5)$$

By taking integrals along the arc of an ellipse, the field contributions from arc segments will contain incomplete elliptic integrals (IEIs) that must be computed numerically. The three kinds of IEIs employed in the results of this study are represented as Legendre's forms with *amplitude z*, *parameter m*, and *characteristic n*. Legendre's first IEI form used here is

$$F(z|m) = \int_0^z \frac{dt}{\sqrt{1 - m \sin^2 t}}. \quad (6)$$

Legendre's second IEI form is

$$E(z|m) = \int_0^z \sqrt{1 - m \sin^2 t} \, dt. \quad (7)$$

Finally, Legendre's IEI of the third form is

$$\Pi(n; z|m) = \int_0^z \frac{dt}{(1 - n \sin^2 t)\sqrt{1 - m \sin^2 t}}. \quad (8)$$

Much of the literature concerning IEI defines them with the *parameter m* bounded to $0 \leq m \leq 1$ [11]–[13], [14, Sec. 19.2(ii)]. The field solutions presented below, however, contain negative *parameters*. By using the imaginary modulus transform, one may extend the domain of m to the entire negative axis [14, eq. 19.7.5]. Several scientific-computing libraries that implement this and other argument transforms, allowing these IEIs with negative m to be accurately computed while still returning real-valued results, are available (see [15], [16]).

B. Radial Segment Solution

Our solution for a radial segment is similar in form to [7] but simple and accurate, in general, not simple in the near-field

$$\vec{B}_{i,\mathrm{rad}}^{\mathrm{seg}}(\vec{r}) = -\frac{\mu_0}{4\pi} V(\vec{r}; \vec{r}') \Big|_{\theta'=\theta_i} \Big|_{z'=z_1}^{z_2} \Big|_{r'=r_1}^{r_2} \quad (9)$$

where the radial component of $V(\vec{r}; \vec{r}')$ is given by

$$\widehat{r} \cdot V(\vec{r}; \vec{r}') = \sin \varphi \, \log(G(\vec{r}; \vec{r}')^{-1} + r' - r \cos \varphi) \quad (10)$$

the azimuthal component is given by

$$\widehat{\theta} \cdot V(\vec{r}; \vec{r}') = \cot \varphi \, (\widehat{r} \cdot V(\varphi, \zeta, \rho)) \quad (11)$$

and, finally, the axial component is given by

$$\widehat{z} \cdot V(\vec{r}; \vec{r}') = \tan^{-1} \left(\frac{\zeta(r' - r \cos \varphi)G(\vec{r}; \vec{r}')}{r \sin \varphi} \right). \quad (12)$$

C. Arc Segment Solution

Algebraically manipulating the surface integral components into elliptic integral forms leads to our solution for arc segments

$$\vec{B}_{i,j,\mathrm{arc}}^{\mathrm{seg}}(\vec{r}) = \frac{\mu_o}{4\pi} W(\vec{r}; \vec{r}') \Big|_{r'=r_j} \Big|_{z'=z_1}^{z_2} \Big|_{\theta'=\theta_{i,1}}^{\theta_{i,2}} \quad (13)$$

where the radial component of $W(\vec{r}; \vec{r}\,')$ is given by

$$\hat{r} \cdot W(\vec{r}; \vec{r}\,') = \frac{\sqrt{(r - r')^2 + \zeta^2}}{r}$$
$$\times \left(E\left(\frac{\varphi}{2} \Big| m \right) - \frac{2 - m}{2} F\left(\frac{\varphi}{2} \Big| m \right) \right) \quad (14)$$

the azimuthal component is given by

$$\hat{\theta} \cdot W(\vec{r}; \vec{r}\,') = \frac{1}{r} G(\vec{r}; \vec{r}\,')^{-1} \quad (15)$$

and, lastly, the axial component is given by

$$\hat{z} \cdot W(\vec{r}; \vec{r}\,') = \frac{\zeta}{\sqrt{(r - r')^2 + \zeta^2}}$$
$$\times \left(F\left(\frac{\varphi}{2} \Big| m \right) - \frac{r + r'}{r - r'} \Pi\left(n; \frac{\varphi}{2} \Big| m \right) \right) \quad (16)$$

with a common *parameter m* for the IEI of

$$m = \frac{-4rr'}{(r - r')^2 + \zeta^2} \quad (17)$$

and a *characteristic n* of

$$n = \frac{-4rr'}{(r - r')^2}. \quad (18)$$

D. Total Solution

The field contribution from a ring's sector i is derived using the superposition principle as in (19) and scaled by a magnetization factor M_i. This includes two arc and two radial segments. For a disk magnet, only one arc segment and two radial segments must be included to form the bounds of the sector

$$\vec{B}_i^{\text{sec}} = M_i \left(\vec{B}_{i,1,\text{rad}}^{\text{seg}} + \vec{B}_{i,2,\text{arc}}^{\text{seg}} - \vec{B}_{i,2,\text{rad}}^{\text{seg}} - \vec{B}_{i,1,\text{arc}}^{\text{seg}} \right). \quad (19)$$

The total field solution from a permanent magnet ring or disk is the superposition over all p sectors, or pole-pairs, as

$$\vec{B}(\vec{r}) = \sum_{i=1}^{p} \vec{B}_i^{\text{sec}}(\vec{r}). \quad (20)$$

For systems evolving in time, this magnetization factor may be used to account for the constitutive law of magnets and effects such as changing magnetization and hysteresis in the presence of a homogeneous external field. For example, using the discretized Preisach or differential Jiles–Atherton hysteresis models, one may evolve the magnetization of each sector in time as a function of an applied external field that is homogeneous over the sector.

E. Similarities and Deviations From Prior Closed-Form Models

Ausserlechner's assumptions about ME geometries resulted in small contributions from arc segments, and so they were ignored in this article. The $\hat{z}$ component from a radial segment that is presented here, however, is the same [7]. The $\hat{r}$ component from a radial segment, as well as the $\hat{\theta}$ component from both segment types are found in portions of the solution presented in [1]. $\hat{r}$ and $\hat{z}$ components from arc segments

introduced here avoid physically unrealistic solutions with imaginary-valued components and produce values that directly correspond to other real-valued results that were numerically derived in the previous work. Furthermore, the case of a single pole-pair cylindrical magnet of the solutions presented here agree with the special case solution for a cylindrical current sheet presented in [10].

F. Notes on Computation

The proposed implementation of the field solution takes around 1 s on a single core of an Intel Core i7-7600 CPU running at 2.8 GHz for 40 points of simulation. Computation of (8), using the Carlson symmetric form and duplication method [16], [17], is the major contributor to this time, taking one-to-two orders of magnitude longer than the computation of the other IEI and elementary functions. Recent investigations into the computational methods for the IEI in Legendre's forms have introduced new methods for simultaneously computing arbitrary linear combinations of the three forms with significant speed increases [18], and all portions of the solution lend themselves well to parallelization, introducing the possibility of implementing these solutions in near-real-time applications.

Since magnetization is a scaling factor on the individual sectors, the field for a ring magnet's sector can be precomputed over a desired range of space and arbitrarily scaled to quickly estimate or explore the effects of magnetization asymmetries. Avoiding extraneous computation of (8) helps save considerable time when iterating over designs.

G. Analysis

The solutions presented here allow for the analysis of non-idealities in magnet construction related to asymmetric sector magnetization and geometry. It is important to note that the equivalent current sheet approach used here, however, does not easily allow for evaluation of more complex non-idealities including, but not limited to, low permeability materials, magnetization angle variation, or inhomogeneous magnetization. Nevertheless, the non-idealities that can be covered are useful for modeling major characteristics of the field as they change in space around the magnet. Furthermore, although this method cannot directly account for highly permeable materials in the vicinity of the magnet, the method of magnetic images may be used to approximate the effects of highly permeable materials in the space [8].

Simulations were carried out for a $p = 4$ pole-pair ring with symmetric sector widths and geometric parameters that closely correspond to the real-world magnet extracted from a standard residential water meter measured in Section III-B

$$r_2 = 11.1 \, \text{mm}, \quad r_1 = 2.73 \, \text{mm}, \quad z_2 = 4.57 \, \text{mm}, \quad z_1 = 0.0 \, \text{mm}. \quad (21)$$

Measurement positions were chosen to analyze cases where near-field assumptions presented in previous works [7] no longer hold and can be found in Table I, except for θ which was simulated over the entire range $0 \le \theta \le 2\pi$ for all cases. Thus, these simulations are directly applicable as a tool for

TABLE I

ANALYSIS SIMULATION PARAMETERS

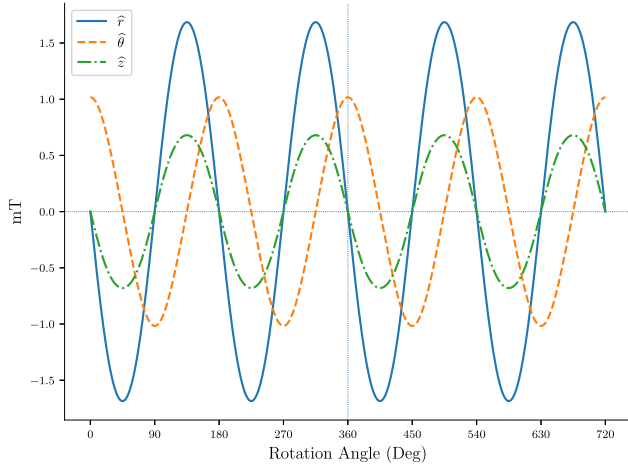|	S_1	S_2	S_3	S_4
r	$2r_2$	$0 \rightarrow 2r_2$	$2r_2$	$0 \rightarrow 4r_2$
z	$3z_2$	$2z_2$	$0 \rightarrow 8z_2$	$2z_2$

Fig. 2. Magnetic-flux density versus rotational angle in S_1 with symmetric magnetization.

the design of a far-field retrofit measurement system for an existing magnetic mechanical system.

A magnetization of 4.3×10^5 A $\cdot$ m^{-1} is used for all simulations, with a scaling factor for each pole-pair of $[-1.05, 1.1, -0.8, 1.1]$ when plotting asymmetric magnetization. For the purposes of this analysis, we will consider the variance of the magnitude difference between adjacent pole-pair magnetizations

$$\text{Var}(\Delta M_i) = \text{Var}(|M_i - M_{i-1}|) \qquad (22)$$

to be a metric for magnetization asymmetry.

Figs. 2 and 3 show the field solutions over S_1 and two rotations of the ring, with symmetric and asymmetric magnetization, respectively. Particularly visible in the asymmetric case are two major harmonics occurring at periods of π and of 2π. We will refer to harmonic with a period of $4\pi/p$ or a spatial period of $2/p$ magnet revolutions as the field fundamental (FF) since it corresponds to the major harmonic content of the sinusoidally varying field. The harmonic with a period of 2π corresponds to the major harmonic over an entire revolution of the magnet, and so will be referred to as the mechanical fundamental (MF). The symmetrically magnetized case still contains frequency content at the MF, but it is smaller relative to the FF than in the asymmetric case.

In general, the lower-frequency MF at the spatial period of the physical disk is the second largest harmonic in the field and is amplified in the presence of asymmetric magnetization. Higher order harmonics in the field occur at multiples of the FF and grow in magnitude relative to the FF and MF, as one moves nearer to null points in the field where the FF and MF are canceled out.

Because the $\widehat{\theta}$ component peaks near the sector's azimuthal boundaries, the other components peak near the azimuthal center of the sector. The FF of the $\widehat{\theta}$ component is nearly
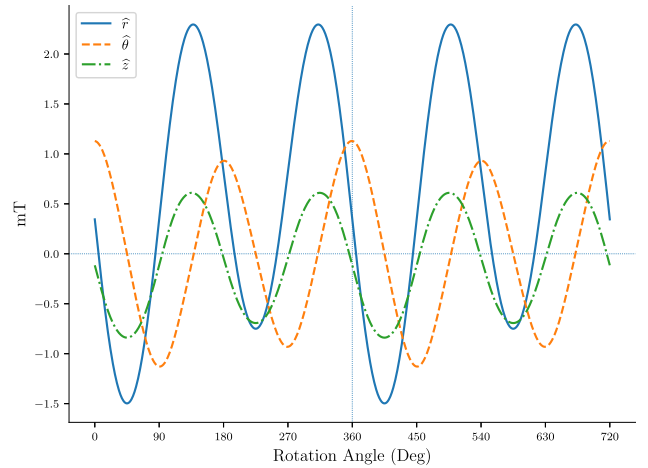

Fig. 3. Magnetic-flux density versus rotational angle in S_1 with asymmetric magnetization.

in quadrature with the FF of the $\widehat{r}$ and $\widehat{z}$ components. As the simulated waveforms and nonlinear solution of the field components demonstrate, however, the separate components are not truly in quadrature. Nevertheless, using a magnetic field sensor and a ring permanent magnet have proven to be a valuable technique for constructing ME rotary position sensors, using either two magnetic field sensors at the orthogonal positions [19]–[21] or a single magnetic field sensor able to measure fields in at least two orthogonal directions [22], [23].

Since sampling the field in one direction but at two positions offset by a quarter field period, or in two directions at one location, gives two sinusoidal signals V_s and V_c with a phase offset close to $\pi/2$ rad, the arctan2 of the field measurements can be used to estimate the rotational position of the disk. After removing dc bias and scaling the amplitudes of measured waveforms, arctan2 produces a reasonable estimate of the phase of the field φ_b and thereby the rotational position of the magnet θ_d. For the purposes of this analysis, we will only consider the latter case of sampling the field at one position, but in two directions. θ_d will correspond to φ_b by

$$\theta_d = \frac{2}{p}\varphi_b = \frac{2}{p}\text{arctan2}\left(\frac{\widetilde{V}_s}{\widetilde{V}_c}\right) \qquad (23)$$

where $\widetilde{V}_c$ and $\widetilde{V}_s$ are the dc bias and amplitude corrected field measurements in the leading and lagging component directions of a designers choice, respectively.

Considerable attention has been paid to methods for characterizing and correcting the errors resulting from this method, either with lookup tables and careful calibration [19]–[23] or through automatic means limited to nearly ideal and/or continuously excited systems [24], [25]. These corrected position estimates find use in a variety of applications including motor control, process monitoring, and equipment diagnostics.

The types of error impacting ME position estimation reduce to amplitude imbalance, nonorthogonal phase, dc field offsets, and extraneous field harmonics in the measured signals [20]. This section explores the contributions to these types of error by sensor positioning and magnetization asymmetries using the solution presented in this article.
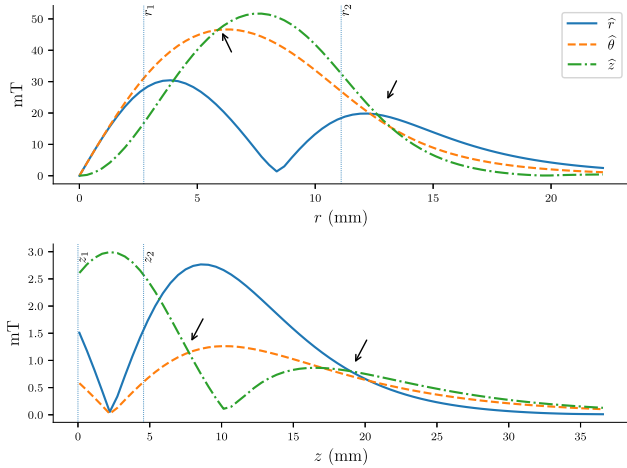
Fig. 4. Sinusoidal field amplitude versus radial distance r in S_2 and axial distance z in S_3 (amplitude balance points indicated by arrows).

Fig. 5. Negative frequency content versus r- and z-axis rotation in S_1 with symmetric and asymmetric magnetization.

1) Amplitude Imbalance: Amplitude imbalance refers to the difference in sinusoidal amplitude over an entire rotation of the quadrature fields produced by an ME. The individual components of the solution contributed by radial and arc segments are different in magnitude, so the superposition over an entire real-world magnet will produce orthogonal field components with inherent amplitude imbalances everywhere in space, except in specific near-field geometries [7] or a few ideal points in the field.

Simulations S_2 and S_3 were carried out over sweeps along the $\widehat{r}$- and $\widehat{z}$-directions, listed in Table I, and their sinusoidal amplitudes over a full rotation were calculated. Fig. 4 shows regions of measurement in which the quadrature pairs come into and out of amplitude balance. The $(\widehat{\theta}, \widehat{z})$ quadrature pair has two points along the axes of simulation that minimize the amplitude imbalance while maximizing individual component amplitude. The $(\widehat{r}, \widehat{\theta})$ pair, however, has only one such point along each axis of simulation, as the closer of the two points of balance occurs near a null in the field. All these balance points are relatively close to the magnet and may not be valid sensor positions for some applications. In this case, designers must use different metrics for optimization and signal processing for compensating amplitude imbalances to reduce error in an angle estimation algorithm.

Asymmetric magnetization will slightly shift the amplitude balance points in space; however, the overall trends and regions of balance will remain the same. In particular, asymmetric magnetization will play a larger role near null points in the field, as the FF is canceled out and the higher order harmonics play a larger role in total amplitude, but these points are less suitable for measurement applications.

Since multiple-axis, magnetic field sensors may have different sensitivities per axis, this model also presents an avenue for balancing their amplitudes with the geometry of the setup, avoiding reliance on signal processing and calibration. A sensor with a stronger sensitivity in $\widehat{r}$ than $\widehat{\theta}$ may benefit from moving out from the $z \approx 18$ mm crossover point to balance the measured amplitudes.

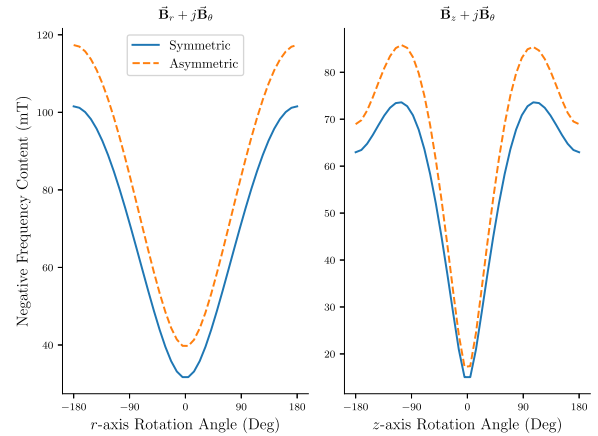*2) Nonorthogonal Phase:* The angle estimation technique described above relies on the two signals being separated in phase by $\pi/2$ rad. Any phase difference on top of this is considered the nonorthogonal phase and contributes to second-order harmonic error in phase estimates [20]. Forming an analytic signal with the two measured signals allows one to use negative frequency content as a measure of nonorthogonality.

The nonorthogonal phase is inherent to the field, considering its nonlinear solution, but sensor rotation has been found to be a larger contributor. As a sensor's Cartesian axes deviate from the cylindrical coordinate axes of the magnet, mixing of the separate components causes the phase difference between the field components to decrease.

Fig. 5, resulting from simulation S_1, demonstrates increasing negative frequency content as the sensor's basis is rotated relative to a magnet's cylindrical basis. This presents an opportunity for correcting sensor rotation using negative frequency content as a metric for reducing the nonorthogonal phase between quadrature field components. Correction for this rotation may be accomplished using standard linear algebra rotation matrices [26]. Asymmetric magnetization contributes to the minimum achievable negative frequency content but does not shift the minimum point.

3) DC Field Offsets: For a magnetized ring with symmetric geometry and an average magnetization of 0, the $\widehat{r}$ and $\widehat{z}$ fields' dc bias will cancel out. The $\widehat{\theta}$ field will have a small amount of bias that scales with asymmetric magnetization, but it will be at least one order of magnitude less than its amplitude.

DC bias, normalized by the remainder of the frequency spectrum, in the $\widehat{r}$ and $\widehat{z}$ components will grow as asymmetry increases. For the $\widehat{\theta}$ field, certain forms of asymmetric magnetization result in decreased amplitude-normalized dc bias and no magnetization configurations were found where dc bias exceeds 10% of the amplitude.

Similar trends were found for positions increasing along $\widehat{r}$ and $\widehat{z}$ so only the former is presented in Fig. 6 using S_4 as an example. These plots can be used for determining optimal places of minimum dc bias for a given direction. For example, $r \approx 12$ mm contains a local minimum in the dc bias in the $\widehat{r}$ field that also reduces dc bias in the $\widehat{\theta}$ field and is conveniently near a point of amplitude balance in Fig. 4.
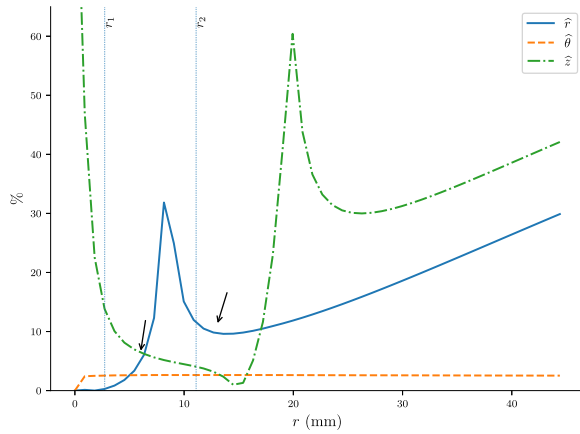
Fig. 6. Normalized dc bias versus radial distance r in S_4 with asymmetric magnetization (bias minimization and amplitude balance points indicated with an arrow).

Fig. 7. Field harmonic magnitude versus radial distance r in S_2.

Fig. 8. FF harmonic magnitude ratio versus radial distance r in S_2.

DC field offsets may lead to sensor saturation in the extreme but lead to second-order harmonic errors in smaller quantities [20]. Barring extreme cases, they can be compensated with careful offset calibration of the sensor and/or software correction at the time of construction. There are already sensor temperature and external field compensation techniques, but asymmetrical demagnetization from thermal, mechanical, or electromagnetic effects will contribute to errors stemming from this bias over time.

4) Extraneous Field Harmonics: Apart from the inherent sensor and field nonlinearities, any present magnetization or geometric asymmetries will contribute to extraneous harmonic content (EHC) in measured signals. Taking the fast Fourier transform (FFT) of the field over a full rotation, the magnitude of the FF and MF can be found at frequencies $p/2$ and 1, respectively. The EHC is defined as the sum of the spectral content at all other frequencies, excluding dc, which can be compensated for in software. The MF is not included in the EHC because the MF may be used by certain estimation techniques to further improve angle tracking. Principally, magnetization asymmetries shift the peaks and nulls of the field produced by individual tiles so that they vary in amplitude and phase relative to each other. This space-varying amplitude modulation adds harmonics to the field and leads to a similar harmonic modulation of angle estimation error [20].

Fig. 7 shows the FF, MF, and EHC content as a function of position in S_2. Significant non-zero FF content always exceeds the MF and EHC content, making it by far the most pronounced and useful signal harmonic for angle estimation. Fig. 8 shows the ratio of the FF harmonic content to the total harmonic content, also in S_2. It shows how the FF harmonic content ratio, however, drops considerably at certain points, in particular, for the $\widehat{r}$ and $\widehat{z}$ components.

For methods tracking the FF and the other present harmonics, these harmonic content metrics provide an avenue for increasing overall harmonic content. For angle estimation methods tracking the FF directly, the normalized FF metric may be used to minimize extraneous harmonic modulation in the estimates. Sensor rotation mixes the effects between the
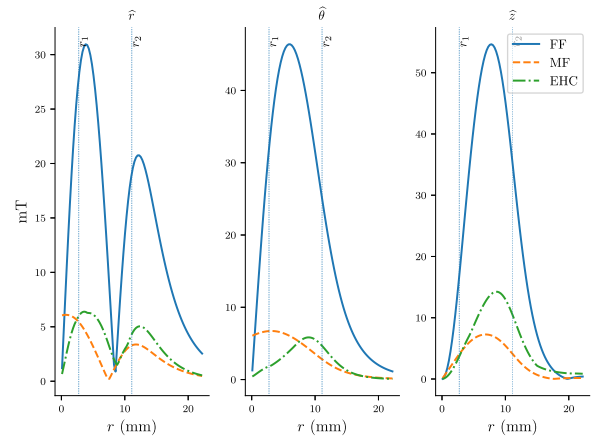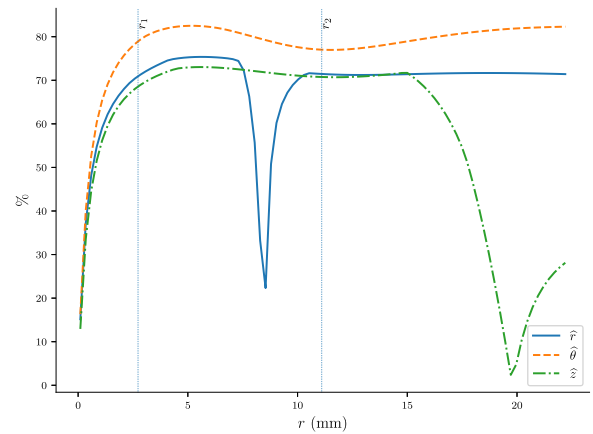
components and asymmetrically changing magnetization will contribute to increasing error in the angle measurement as the harmonics deviate from any available calibration data.

III. RESULTS

This section first verifies the solution against the work in previous literature by direct comparison to reported results. The fields from two magnetic rings were measured as a secondary confirmation of the solution's accuracy and usefulness as a design and verification tool for realistic, e.g., asymmetrical, magnets.

A. Previous Works Verification

Furlani and Knewtson [8] and Furlani [9] provided FEA-verified numerical solutions for various magnetic ring configurations. We simulated two of their example geometries, which cover all field component directions, using our field solutions and plotted the results against digitized results from their simulation and FEA analysis in Figs. 9 and 10. As the first example geometry is a single pole-pair ring magnet, we also used the simplified arc segment solution from [10] as a comparison. Its parameters can be found under $D_{s,1}$ in Table II. The second example ring's geometric parameters can be found under $D_{s,2}$. For both geometries, we used a magnetization of 4.3×10^5 A · m^{-1} for each sector.
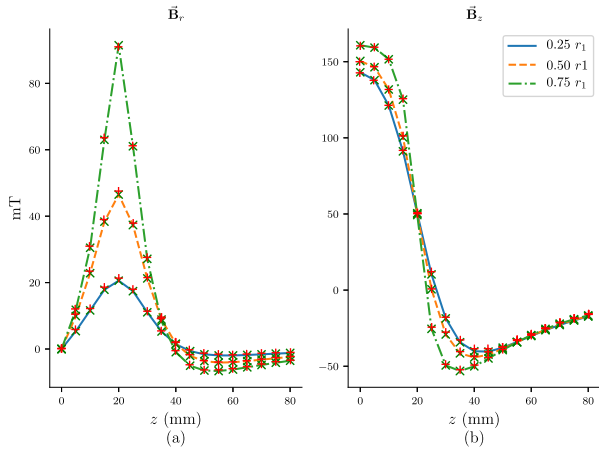
Fig. 9. $D_{s,1}$ simulation versus reference data from (a) Fig. 3 and (b) Fig. 4 in [9] and the arc segment solutions in [10] (+ = reference data, x = arc segment solution).
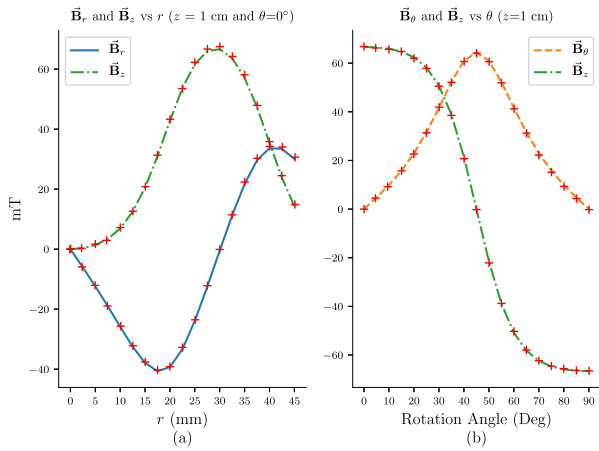

Fig. 10. $D_{s,2}$ simulation versus reference data from (a) Fig. 5 and (b) Fig. 6 in [9] (+ = reference data).

TABLE II
GEOMETRIC DIMENSIONS FOR SIMULATED RINGS

	$D_{s,1}$	$D_{s,2}$	D_1	D_2
p	1	4	8	4
r_2 (mm)	40	40	9.53	11.1
r_1 (mm)	20	20	5.99	2.73
z_2 (mm)	20	0	3.00	4.57
z_1 (mm)	−20	−10	0.00	0.00
$\Delta\theta°$	360	90	45	—
$\Delta\theta_1°$	—	—	—	82.6
$\Delta\theta_2°$	—	—	—	97.3
$\Delta\theta_3°$	—	—	—	82.6
$\Delta\theta_4°$	—	—	—	97.3

In all cases, our simulation results matched exactly, barring manual digitization errors.

B. Experimental Verification

To validate the results with real-world data, two permanent magnets' fields were recorded on a test bed for measuring

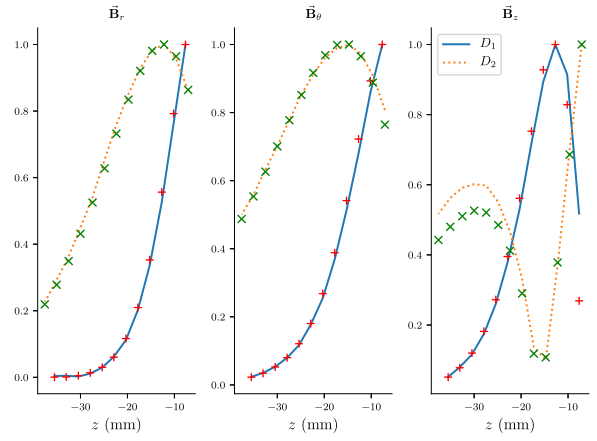

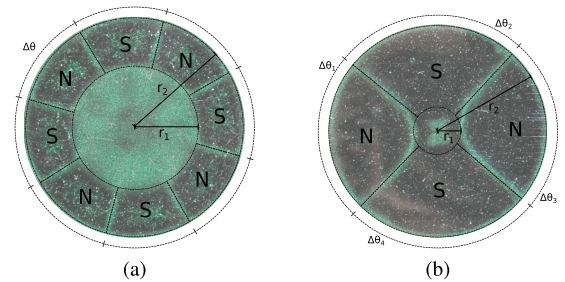Fig. 11. Normalized FF magnitude of measured fields (+, x = simulated data).

Fig. 12. (a) D_1 and (b) D_2 annotated geometry, viewed through magnetic viewing film.

the magnetic flux density at fixed (r, z) positions over a full rotation $0 \leq \theta_d \leq 2\pi$ of the magnet. The test bed employs an MLX90393 three-axis Hall effect sensor produced by Melexis [27], an example of a magnetic-flux density sensor that is applicable for very cost-sensitive applications that require high sensitivity, such as in retrofit of existing magnetic structures for real-time position measurement.

The first magnet, D_1, was a nearly uniform neodymium ring magnet measured at an r of 27.9 mm over a sweep of z-heights. The second magnet, D_2, sourced from the magnetic coupler within a standard residential water meter, diverged considerably from our model's geometry and was measured at an r of 41.6 mm over the same z-height sweep. The geometric parameters used for simulation were physically measured and are listed in Table II.

As a figure of merit, we extracted the FF's magnitude from simulated and measured fields and plotted it against decreasing z-height for each component in Fig. 11. The FF is the major harmonic used in the angle estimation procedure described in Section II-G and, thus, is a signal of interest for these applications. To account for variations in sensor sensitivity and other measurement errors, the magnitude was normalized with respect to its maximum value over the sweep.

1) Magnet Example D_1: D_1 features symmetric magnetization boundaries, manufacturer provided geometric data, and strong coercivity and magnetization. Although these features make D_1 an ideal candidate for measurement, it does not,

in fact, have perfectly symmetric magnetization strengths resulting in considerable spectral content outside the FF. Furthermore, the measurement setup experienced slight eccentricity in the magnet's rotational axis. The effects of this are magnified in the near-field, explaining deviations in our metric as the sensor moved closer to the magnet. The trends, however, still follow closely.

2) Magnet Example D_2: D_2 diverges more strongly from our model. Its magnetization pattern can only be approximately modeled by cylindrical tile sectors, is less homogeneous near its center, and is formed from a material with less coercivity. Thus, D_2's magnetizations and sector boundaries were not considered to be uniform for simulation. Instead, we used photo measurement software to approximate sector widths from Fig. 12(b). Even with increasing sources of error from measurement, fitting, and geometry nonideality, the trends still closely follow, verifying the correctness of field solutions presented here and demonstrating their usefulness in optimizing measurement position, even for permanent magnet disks with geometries that diverge from the model.

IV. Conclusion

This article presents an easily computable, real-valued, 3-D field solution for axially polarized multi-pole ring and disk magnets. When combined with solutions for diametrically polarized magnets [28], one now has access to a toolbox for designing, evaluating, and measuring a wide range of electromechanical structures. This approach avoids FEA, or other highly application-tailored and numerical, analysis techniques.

There are many different quantities that may be derived from this model, such as the torque and slip between the magnet and an external field [3], [4], [29]. Furthermore, using superposition, one may analytically model even more complicated geometries composed of combinations of cylindrical sectors, such asymmetrical skewed cylindrical sectors. Combining these two techniques with the method of magnetic images allows for the analyzing, designing, and optimizing of new magnetic structures, e.g., asymmetrically skewed axial flux permanent magnet motors, where computationally expensive FEA over a large number of topologies was required before [30], [31].

ACKNOWLEDGMENT

References

[1] R. Ravaud, G. Lemarquand, and V. Lemarquand, "Magnetic field created by tile permanent magnets," *IEEE Trans. Magn.*, vol. 45, no. 7, pp. 2920–2926, Jul. 2009.

[2] R. Ravaud, G. Lemarquand, V. Lemarquand, and C. Depollier, "Analytical calculation of the magnetic field created by permanent-magnet rings," *IEEE Trans. Magn.*, vol. 44, no. 8, pp. 1982–1989, Aug. 2008.

[3] R. Ravaud, G. Lemarquand, and V. Lemarquand, "Ironless permanent magnet motors: Three-dimensional analytical calculation," in *Proc. IEEE Int. Electric Machines Drives Conf.*, May 2009, pp. 947–952.

[4] R. Ravaud, G. Lemarquand, V. Lemarquand, and C. Depollier, "Permanent magnet couplings: Field and torque three-dimensional expressions based on the Coulombian model," *IEEE Trans. Magn.*, vol. 45, no. 4, pp. 1950–1958, Apr. 2009.

[5] R. Ravaud, G. Lemarquand, and V. Lemarquand, "Magnetic field created by a uniformly magnetized tile permanent magnet," *Prog. Electromagn. Res. C*, vol. 24, pp. 17–32, Jul. 2010.

[6] G. Lemarquand, V. Lemarquand, S. Babic, and C. Akyel, "Magnetic field created by thin wall solenoids and axially magnetized cylindrical permanent magnets," in *Proc. Progr. Electromagn. Res. Symp.*, Moscow, Russia, 2009, p. 614.

[7] U. Ausserlechner, "Closed analytical formulae for multi-pole magnetic rings," *Prog. Electromagn. Res. B*, vol. 38, pp. 71–105, Jan. 2012.

[8] E. Furlani and M. Knewtson, "A three-dimensional field solution for permanent-magnet axial-field motors," *IEEE Trans. Magn.*, vol. 33, no. 3, pp. 2322–2325, May 1997.

[9] E. Furlani, "A three-dimensional field solution for axially-polarized multipole disks," *J. Magn. Magn. Mater.*, vol. 135, no. 2, pp. 205–214, Jul. 1994.

[10] L. Urankar, "Vector potential and magnetic field of current-carying finite arc segment in analytical form, part II: Thin sheet approximation," *IEEE Trans. Magn.*, vol. 18, no. 3, pp. 911–917, May 1982.

[11] E. W. Weisstein. *Elliptic Integral of the First Kind*. Accessed: Aug. 16, 2019. [Online]. Available: http://mathworld.wolfram.com/EllipticIntegraloftheFirstKind.html

[12] E. W. Weisstein. *Elliptic Integral of the Second Kind*. Accessed: Aug. 16, 2019. [Online]. Available: http://mathworld.wolfram.com/EllipticIntegraloftheSecondKind.html

[13] E. W. Weisstein. *Elliptic Integral of the Third Kind*. Accessed: Aug. 16, 2019. [Online]. Available: http://mathworld.wolfram.com/EllipticIntegraloftheThirdKind.html

[14] B. C. Carlson. *Elliptic Integrals*. in NIST Digital Library of Mathematical Functions (Release 1.0.23 of 2019-06-15). Accessed: Aug. 16, 2019. [Online]. Available: https://dlmf.nist.gov/19

[15] P. Virtanen *et al.*, "SciPy 1.0–fundamental algorithms for scientific computing in python," Jul. 2019, *arXiv:1907.10121*. [Online]. Available: https://arxiv.org/abs/1907.10121

[16] F. Johansson. (Dec. 2018). *mpmath: A Python Library for Arbitrary-Precision Floating-Point Arithmetic (version 1.1.0)*. Accessed: Mar. 27, 2019. [Online]. Available: http://mpmath.org/

[17] F. Johansson, "Numerical evaluation of elliptic functions, elliptic integrals and modular forms," in *Elliptic Integrals, Elliptic Functions and Modular Forms in Quantum Field Theory*, J. Blümlein, C. Schneider, and P. Paule, Eds. Cham, Switzerland: Springer, 2019, pp. 269–293.

[18] T. Fukushima, "Precise and fast computation of a general incomplete elliptic integral of third kind by half and double argument transformations," *J. Comput. Appl. Math.*, vol. 236, no. 7, pp. 1961–1975, Jan. 2012.

[19] S. Hao, Y. Liu, and M. Hao, "Study on a novel absolute magnetic encoder," in *Proc. IEEE Int. Conf. Robot. Biomimetics*, Feb. 2009, pp. 1773–1776.

[20] Q. Lin, T. Li, and Z. Zhou, "Error analysis and compensation of the orthogonal magnetic encoder," in *Proc. 1st Int. Conf. Instrum., Meas., Comput., Commun. Control*, Oct. 2011, pp. 11–14.

[21] X. Wang, H. Wang, H. Xie, D. Lou, and K. Yang, "Design of magnetic encoder based on reconstructing and mapping looking-up table," in *Proc. 19th Int. Conf. Elect. Mach. Syst. (ICEMS)*, Nov. 2016, pp. 1–4.

[22] M. Blagojevic, N. Markovic, and R. S. Popovic, "Testing the homogeneity of magnets for rotary position sensors," *IEEE Trans. Magn.*, vol. 50, no. 11, pp. 1–5, Nov. 2014.

[23] *Allegro MicroSystems–Advanced On-Chip Linearization in the A1335 Angle Sensor IC*. Accessed: Mar. 27, 2019. [Online]. Available: https://www.allegromicro.com/es-ES/Design-Center/Technical-Documents/Hall-Effect-Sensor-IC-Publications/Advanced-On-Chip-Linearization-A1335-Angle-Sensor-IC.aspx

[24] S. Balemi, "Automatic calibration of sinusoidal encoder signals," *IFAC Proc. Volumes*, vol. 38, no. 1, pp. 68–73, 2005.

[25] X. Guo and M. Bodson, "Frequency estimation and tracking of multiple sinusoidal components," in *Proc. 42nd IEEE Int. Conf. Decis. Control*, vol. 5, Jun. 2004, pp. 5360–5365.

[26] Z. Zhang, C. Xiao, K. Yin, and H. Yan, "A magnetic field correction method for the non-ideally placed 3-axial magnetometer sensor," in *Proc. Int. Conf. Measuring Technol. Mechatronics Autom.*, vol. 1, Mar. 2010, pp. 130–133.

[27] *MLX90393 Triaxis Magnetic Node*. Accessed: Mar. 29, 2019. [Online]. Available: https://www.melexis.com/-/media/files/documents/datasheets/mlx90393-datasheet-melexis.pdf

[28] V. T. Nguyen and T.-F. Lu, "Analytical expression of the magnetic field created by a permanent magnet with diametrical magnetization," *Progr. Electromagn. Res. C*, vol. 87, pp. 163–174, Sep. 2018.

[29] R. Ravaud, V. Lemarquand, and G. Lemarquand, "Analytical design of permanent magnet radial couplings," *IEEE Trans. Magn.*, vol. 46, no. 11, pp. 3860–3865, Nov. 2010.

[30] H. Xie *et al.*, "Research of asymmetrical bidirectional magnet skewing technique in modular multi-stage axial flux permanent magnet synchronous motor," *IEEE Trans. Magn.*, vol. 51, no. 3, pp. 1–5, Mar. 2015.

[31] M. Gulec and M. Aydin, "Magnet asymmetry in reduction of cogging torque for integer slot axial flux permanent magnet motors," *IET Electr. Power Appl.*, vol. 8, no. 5, pp. 189–198, May 2014.

Eric A. Ponce received the B.S. degree and the M.Eng. degree from the Massachusetts Institute of Technology, Cambridge, MA, USA, in 2017 and 2019, respectively, where he is currently pursuing the Ph.D. degree.

Steven B. Leeb (Fellow, IEEE) received the doctoral degree from the Massachusetts Institute of Technology (MIT), Cambridge, MA, USA, in 1993.

He has served as a Commissioned Officer for the USAF Reserves. He has been a Faculty Member with the Department of Electrical Engineering and Computer Science, MIT, since 1993. He also holds a joint appointment with the Department of Mechanical Engineering, MIT. He is the author or coauthor of over 150 publications and holds 20 U.S. patents in the fields of electromechanics and power electronics.